A pressure-correction scheme for convection-dominated incompressible flows with discontinuous velocity and continuous pressure

Lorenzo Botti, Daniele Antonio Di Pietro

A pressure-correction scheme for convection-dominated incompressible flows with discontinuous velocity and continuous pressure

Lorenzo Botti[*,a,b], Daniele A. Di Pietro[c]

[a] *Biomedical Engineering Department, Mario Negri Institute for Pharmacological Research, Bergamo, Italy*
[b] *Industrial Engineering Department, University of Bergamo, Italy*
[c] *Insitut Français du Pétrole, 1& 4 avenue Bois Préau, 92852 Rueil-Malmaison, France*

Abstract

In this work we present a pressure-correction scheme for the incompressible Navier-Stokes equations combining a discontinuous Galerkin approximation for the velocity with a standard continuous Galerkin approximation for the pressure. The main interest of pressure-correction algorithms is the reduced computational cost compared to fully coupled schemes. The aim of the present work is to show how a proper discretization of the decoupled momentum equation can render this method suitable to simulate high Reynolds regimes. The proposed spatial velocity-pressure approximation is LBB stable for equal polynomial orders and it allows adaptive p-refinement for velocity and global p-refinement for pressure. The method is validated against a large set of classical two- and three-dimensional test cases covering a wide range of Reynolds numbers, in which it proves effective both in terms of accuracy and computational cost.

Key words:
Incompressible Navier-Stokes equations, Discontinuous Galerkin, Pressure-Correction

[*]Send correspondence to Lorenzo Botti, viale Marconi 5 - 24044 Dalmine (BG) Fax:+39 035 2052077, Tel:+39 035 2052084, email:lorenzo.botti@unibg.it

1. Introduction

Discontinuous Galerkin (dG) methods offer effective means to obtain accurate discretizations of complex problems on general meshes. In this work, we deal with advection-dominated incompressible flows, which constitute a challenging class of problems both in terms of numerical stability and computational cost. In this context, dG methods offer many advantages: LBB stable equal-order discretizations can be devised, the extension to arbitrary unstructured and nonconforming grids is straightforward, and the resulting discretization displays an increased stability in the high Reynolds regimes. Another feature highly appreciated by practitioners in fluid dynamics is that the discretization can be designed so that physical quantities such as momentum or mass are locally conserved. Flexibility, however, comes at a price. In particular, memory requirements as well as the increased computational cost have discouraged wide adoption of these methods up to now. In this work we present an effective strategy to overcome these limitations inspired by classical projection methods.

DG discretizations of the Incompressible Navier-Stokes (INS) equations have been considered in several works. A mixed-order scheme on simplicial meshes has been considered by Girault, Rivière and Wheeler [19], where the authors prove LBB stability for polynomial orders up to the third. More general meshes and equal-order approximation can be dealt with by suitable pressure stabilization techniques. We refer to Cockburn Kanschat, Schötzau and Schwab [8] and to Bassi, Crivellini, Di Pietro and Rebay [4, 5]; see also [12]. Several techniques have been proposed for the discretization of the non-linear advective term. Convergence estimates for a trilinear form with upwind stabilization have been derived by Girault, Rivière and Wheeler [19]. In [8], Cockburn, Kanschat and Schötzau prove the convergence of a fixed point iteration based on the LDG method introduced in [7] to the solution of the INS problem. More recently, Di Pietro and Ern in [13] have proposed a set of sufficient conditions on the trilinear form ensuring convergence to minimal regularity solution.

As regards time marching schemes, splitting methods have also been considered also in conjunction with (fully or partially) discontinuous space discretizations. The original pressure-correction method is due to Chorin and Temam [6, 31]; an incremental form was later proposed by Goda [20], while a second-order incremental scheme is due to Van Kan [32]. In [27] Liu and Shu propose a method for the two-dimensional INS equations in the vortic-

ity stream-function formulation with discontinuous velocity and continuous pressure. In [29], Shahbazi, Fischer and Ethier introduce an effective three-step algebraic splitting dG discretization of the INS equations in primitive variables with explicit treatment of the non-linear term in the advection diffusion step. As noted by Sherwin [24], in high Reynolds incompressible flows, splitting methods can be computationally efficient and competitive in accuracy compared to more expensive coupled methods. As a matter of facts, a coupled velocity and pressure system involves the solution of the saddle point problem induced by the incompressibility constraint, which in turn requires *ad-hoc* preconditioners and has limited applicability to 3D large-scale unsteady simulations. Moreover, in convection-dominated flows, the time step is restricted by stability considerations in the first place, so that the splitting error, scaling as $\Delta t/\mathrm{Re}$ for a first order method, fails to limit the accuracy of the scheme.

In this work we propose a formulation based on the well known pressure-correction scheme featuring discontinuous velocity and continuous pressure. As the space couple is LBB stable for equal- and mixed order discretizations, pressure stabilization is not needed, thereby reducing the coupling between the momentum and the pressure equation. In this configuration we are able exploit the ability of dG to deal with convection-dominated flows maintaining a less expensive Galerkin discretization for the Laplacian operator associated with the pressure projection step. Both the steps of the scheme can be solved with iterative methods employing standard preconditioners, resulting in an effective solution process. To avoid time step restrictions the advection-diffusion step is discretized in time using a fully implicit backward Euler or second-order backward differentiation formula.

2. Solution strategy

The material is organized as follows: §2.1 contains a general overview of projection methods, §2.2 deals with the time discretization and §2.3 with the space discretization.

2.1. Projection Methods

Let $\Omega \subset \mathbb{R}^d$, $d \in \{2, 3\}$, denote a bounded connected open set and let $t_F > 0$. We consider the unsteady INS equations with homogeneous Dirichlet

boundary conditions,

$$\begin{cases} \dfrac{\partial \mathbf{u}}{\partial t} + u_j \nabla_j \mathbf{u} - \nu \nabla^2 \mathbf{u} + \nabla p = \mathbf{f} & \text{in } \Omega \times (0, t_F), \\ \nabla \cdot \mathbf{u} = 0 & \text{in } \Omega \times (0, t_F), \\ \mathbf{u}(x,t) = 0 & \text{for a.e. } x \in \partial\Omega,\ t \in (0, t_F), \\ \mathbf{u}(x,0) = \mathbf{u}_0(x) & \text{for a.e. } x \in \Omega, \\ \int_\Omega p = 0, \end{cases}$$

where $\nu > 0$ denotes the (constant) viscosity, $\mathbf{f}$ is a given body force and u_0 is the initial condition. In the above, we made use of Einstein's convention for repeated indices. The main idea of projection methods is to decouple the incompressibility constraint $\nabla \cdot \mathbf{u} = 0$ from the momentum equation. This strategy is attractive because it only requires to solve an advection-diffusion equation for the velocity and an elliptic equation for the pressure at each time step, thereby lending itself to a more efficient implementation than a fully coupled scheme. The decoupling is achieved by introducing a projection operator onto the space of divergence-free functions,

$$D \stackrel{\text{def}}{=} \{\mathbf{v} \in [L^2(\Omega)]^d \mid \nabla \cdot \mathbf{v} = 0 \text{ in } \Omega,\ \mathbf{v} \cdot \mathbf{n} = 0 \text{ on } \partial\Omega\}.$$

and using the classical decomposition

$$[L^2(\Omega)]^d = D \oplus \nabla(H^1(\Omega)). \tag{1}$$

Equation (1) states that every function $\mathbf{v} \in [L^2(\Omega)]^d$ can be uniquely decomposed into a divergence-free component plus an irrotational one. Denote by $\mathcal{P}_D : [L^2(\Omega)]^d \to D$ the operator that maps every function of $[L^2(\Omega)]^d$ into its divergence free part. For a given $\mathbf{v} \in [L^2(\Omega)]^d$, this projection can be computed by solving the Neumann problem for the potential ϕ

$$\begin{cases} \nabla^2 \phi = \nabla \cdot \mathbf{v}, & \text{in } \Omega, \\ \dfrac{\partial \phi}{\partial \mathbf{n}} = \mathbf{v} \cdot \mathbf{n}, & \text{on } \partial\Omega, \end{cases}$$

and setting

$$\mathcal{P}_D(\mathbf{v}) = \mathbf{v} - \nabla\phi. \tag{2}$$

Applying the divergence operator to the momentum equation and using the divergence-free constraint, we obtain the Poisson equation for the pressure

$$\nabla^2 p = \nabla \cdot (\mathbf{f} - \mathbf{u} \cdot \nabla \mathbf{u}) \qquad \text{in } \Omega \times (0, t_F), \tag{3}$$

while taking the normal component on $\partial\Omega$ and using the homogeneous Dirichlet boundary conditions yields

$$\frac{\partial p}{\partial \mathbf{n}} = \mathbf{n} \cdot (\mathbf{f} + \nu \nabla^2 \mathbf{u}) \qquad \text{on } \partial\Omega \times (0, t_F). \tag{4}$$

The exact pressure satisfies the system (3)-(4). In the context of projection methods, a modified version of this problem is used to obtain a pressure approximation at each time step, as will be discussed in the next section.

2.2. Pressure-correction scheme and time integration

This section addresses the time discretization by the pressure correction method and pinpoints the relation between the semi-discrete formulation and the computation of $\mathcal{P}_D$. More precisely, we consider, for the sake of notation, the incremental form of the pressure-correction with backward Euler time discretization, while a higher-order time discretization will be derived by means of a second-order backward differentiation formula (BDF). We introduce a partition of the time domain $(0, t_F)$ into equally spaced intervals of length Δt and set, for $n > 0$, $t^n \stackrel{\text{def}}{=} n\Delta t$. Let $(\widetilde{\mathbf{u}}^0, \mathbf{u}^0, p^0)$ denote a set of initial guesses and define the sequence of triplets $(\widetilde{\mathbf{u}}^{n+1}, \mathbf{u}^{n+1}, p^{n+1})$ iteratively by solving the following problems:

$$\begin{cases} \dfrac{\mathbf{u}^{n+1} - \widetilde{\mathbf{u}}^n}{\Delta t} - \nu \nabla^2 \mathbf{u}^{n+1} \\ \qquad + (\mathbf{u}^{n+1} \cdot \nabla)\mathbf{u}^{n+1} + \dfrac{1}{2}(\nabla \cdot \mathbf{u}^{n+1})\mathbf{u}^{n+1} + \nabla p^n = \mathbf{f}^{n+1} & \text{in } \Omega, \\ \mathbf{u}^{n+1} = 0 & \text{on } \partial\Omega, \end{cases} \tag{5}$$

and

$$\begin{cases} \dfrac{\widetilde{\mathbf{u}}^{n+1} - \mathbf{u}^{n+1}}{\Delta t} + \nabla(p^{n+1} - p^n) = 0 & \text{in } \Omega, \\ \nabla \cdot \widetilde{\mathbf{u}}^{n+1} = 0 & \text{in } \Omega, \\ \widetilde{\mathbf{u}}^{n+1} \cdot \mathbf{n} = 0 & \text{on } \partial\Omega. \end{cases} \tag{6}$$

(Temam's device [31] has been used in (5) to obtain a skew-symmetric version of the advective term.) Both $\widetilde{\mathbf{u}}^n$ and $\mathbf{u}^n$ represent approximations of the exact velocity at the discrete time t^n. In particular, $\mathbf{u}^n$ accounts for momentum diffusion and advection as well as for the exact boundary condition, whereas $\widetilde{\mathbf{u}}^n$ incorporates the divergence-free constraint. It can be checked that the

projection step (6) is equivalent to setting $\widetilde{\mathbf{u}}^{n+1} = \mathcal{P}_D \mathbf{u}^{n+1}$, thereby showing that the algorithm (5)-(6) belongs to the class of projection methods.

Following Guermond and Quartapelle [21], it is possible to devise formulations which do not require the actual computation of $\widetilde{\mathbf{u}}^n$. As a matter of facts, from the first equation of (6) it is inferred that

$$\widetilde{\mathbf{u}}^n = \mathbf{u}^n - \Delta t \nabla (p^n - p^{n-1}).$$

Plugging the above expression evaluated at discrete times t^n and t^{n-1} into equation (5) yields

$$\begin{cases} \dfrac{\mathbf{u}^{n+1} - \mathbf{u}^n}{\Delta t} - \nu \nabla^2 \mathbf{u}^{n+1} + (\mathbf{u}^{n+1} \cdot \nabla)\mathbf{u}^{n+1} \\ \qquad\qquad + \dfrac{1}{2}(\nabla \cdot \mathbf{u}^{n+1})\mathbf{u}^{n+1} = \mathbf{f}^{n+1} - \nabla(2p^n - p^{n-1}) & \text{in } \Omega, \\ \mathbf{u}^{n+1} = 0 & \text{in } \partial\Omega. \end{cases} \tag{7}$$

Applying the divergence operator to the first equation of (6), the projection step can be reformulated as a Poisson equation for the pressure increment $(p^{n+1} - p^n)$

$$\begin{cases} -\nabla^2 (p^{n+1} - p^n) = -\dfrac{1}{\Delta t} \nabla \cdot \mathbf{u}^{n+1} & \text{in } \Omega, \\ \dfrac{\partial (p^{n+1} - p^n)}{\partial \mathbf{n}} = 0 & \text{on } \partial\Omega. \end{cases} \tag{8}$$

The pressure approximation p^{n+1} can be obtained as a result of the projection process avoiding the direct discretization of problem (3)-(4). However, considering the second equation in (8), we infer that, on $\partial\Omega$,

$$\nabla p^{n+1} \cdot \mathbf{n} = \nabla p^n \cdot \mathbf{n} = \ldots = \nabla p^0 \cdot \mathbf{n} \qquad \text{on } \partial\Omega. \tag{9}$$

This boundary condition is clearly different from the consistent one derived in (4), and it is responsible for the appearance of a spurious boundary layer in the approximate solution (cf. Orszag [28]). It has been demonstrated by Shen [30] and E and Liu [14] that enforcing an artificial boundary condition in a projection method limits the temporal accuracy of the pressure to first order, whereas second order can still be attained for the velocity. In the context of finite element methods, the enforcement of the consistent boundary condition requires either to resort to more expensive projection methods [22] or to adopt alternative formulations [15]. Interestingly enough, however,

due to the presence of viscosity in the right hand side of equation (4), the accuracy loss ascribed to the imposition of the artificial boundary condition (9) decreases with the increase in the Reynolds number. This aspect limits the benefits provided by costly projection formulations when dealing with convection-dominated flows and will be numerically investigated in §3.2.

The final form of the pressure-correction algorithm is obtained replacing the backward Euler scheme by a BDF2, thereby modifying (7) as follows:

$$\begin{cases} \left(\dfrac{\beta_0}{\Delta t} - \nu\nabla^2\right)\mathbf{u}^{n+1} + (\mathbf{u}^{n+1}\cdot\nabla)\mathbf{u}^{n+1} + \dfrac{1}{2}(\nabla\cdot\mathbf{u}^{n+1})\mathbf{u}^{n+1} = \\ \qquad \mathbf{f}^{n+1} - \left(\dfrac{\beta_1}{\Delta t}\mathbf{u}^n + \dfrac{\beta_2}{\Delta t}\mathbf{u}^{n-1}\right) - \nabla(\gamma_1 p^n + \gamma_2 p^{n-1} + \gamma_3 p^{n-2}) & \text{in } \Omega, \\ \mathbf{u}^{n+1} = 0 & \text{on } \partial\Omega, \end{cases} \tag{10}$$

where the coefficients $\beta_0 = 3/2, \beta_1 = -2, \beta_2 = 1/2$ are associated to the BDF2 formula, while taking $\gamma_1 = 7/3, \gamma_2 = -5/3, \gamma_3 = 1/3$ yields a pressure extrapolation computed according to the BDF order (cf., e.g., Guermond, Minev and Shen [22]). To avoid time step restrictions and extrapolations for the non-linear term, equation (10) can be solved by means of the Newton method requiring the computation of the analytic Jacobian associated with each linear iteration. In the same framework equation (8) becomes

$$\begin{cases} -\nabla^2(p^{n+1} - p^n) = -\dfrac{\beta_0}{\Delta t}\nabla\cdot\mathbf{u}^{n+1} & \text{in } \Omega, \\ \dfrac{\partial(p^{n+1} - p^n)}{\partial\mathbf{n}} = 0 & \text{on } \partial\Omega. \end{cases} \tag{11}$$

2.3. Space discretization

The fully discrete problem is based on a discontinuous Galerkin discretization of (7) combined with a standard continuous Galerkin discretization of (8). This choice guarantees LBB stability and it allows to benefit from the favourable properties of dG methods in advection-dominated regimes.

Let $\{\mathcal{T}\}_{h>0}$ denote a shape-regular, quasi-uniform family of simplicial meshes of the domain Ω. The mesh faces are collected in the set $\mathcal{F}_h$ partitioned into $\mathcal{F}_h^i \cup \mathcal{F}_h^b$, where $\mathcal{F}_h^b$ collects the faces located on the boundary of Ω, whereas, for all $F \in \mathcal{F}_h^i$ there exist T_1, $T_2 \in \mathcal{T}_h$, $T_1 \neq T_2$, such that $F = \partial T_1 \cap \partial T_2$. For any function ϕ such that an integrable (possibly two-valued) trace is defined on $F \in \mathcal{F}_h^i$ we let

$$[\![\phi]\!] \stackrel{\text{def}}{=} \phi_{|T_1} - \phi_{|T_2}, \qquad \{\phi\} \stackrel{\text{def}}{=} \frac{1}{2}(\phi_{|T_1} + \phi_{|T_2}).$$

On boundary faces, the jump and average operators are conventionally defined by $[\![\phi]\!] = \{\phi\} = \phi$. Finally, for $F \in \mathcal{F}_h^b$, $\mathbf{n}_F$ represents the unit outward normal to Ω, whereas for $F \in \mathcal{F}_h^i$, $\mathbf{n}_F$ is defined as the unit normal pointing from T_1 to T_2 (the order of the elements sharing F is arbitrary but fixed).

For a given polynomial degree $k \geq 1$, we introduce the following finite dimensional spaces:

$$V_h^k \stackrel{\text{def}}{=} \{v_h \in L^2(\Omega) \mid \forall T \in \mathcal{T}_h,\, v_{h|T} \in \mathbb{P}_d^k(T)\},$$
$$Q_h^k \stackrel{\text{def}}{=} \{q_h \in C^0(\Omega) \mid \forall T \in \mathcal{T}_h,\, q_{h|T} \in \mathbb{P}_d^k(T)\}.$$

The discrete velocity and pressure are sought, respectively, in

$$U_h \stackrel{\text{def}}{=} [V_h^k]^d, \quad P_h \stackrel{\text{def}}{=} Q_h^k/\mathbb{R}.$$

For simplicity of notation we identify equal-order and mixed-order velocity-pressure discretizations respectively as dG(k)-cG(k) and dG(k)-cG($k-1$) (cG standing for "continuous Galerkin").

Diffusive term in the momentum equation. The diffusive term is discretized following Arnold [2], and the k-dependency of the penalty parameter is accounted for as in Georgoulis *et al.* [18]. For all $\mathbf{u}_h$, $\mathbf{v}_h \in U_h$, the corresponding bilinear form is then given by

$$a_h(\mathbf{u}_h, \mathbf{v}_h) \stackrel{\text{def}}{=} \int_\Omega \nabla_{h,j} u_{h,i} \nabla_{h,j} v_{h,i} + \sum_{F \in \mathcal{F}_h} \frac{\eta k^2}{h_F} \int_F [\![\mathbf{u}_h]\!] \cdot [\![\mathbf{v}_h]\!]$$
$$\sum_{F \in \mathcal{F}_h} \int_F \left[\{\nabla_{h,j} u_{h,i}\} [\![v_{h,i}]\!] n_{F,j} + \{\nabla_{h,j} v_{h,i}\} [\![u_{h,i}]\!] n_{F,j} \right],$$

where η is a positive penalty parameter and Einstein's convention has been used for repeated indices.

Nonlinear advective term in the momentum equation. For the advective trilinear form, we follow Di Pietro and Ern [13], where a non-dissipative formulation relying on Temam's device is proposed. For all $\mathbf{w}_h$, $\mathbf{u}_h$, $\mathbf{v}_h \in U_h$ we set

$$t_h(\mathbf{w}_h, \mathbf{u}_h, \mathbf{v}_h) \stackrel{\text{def}}{=} \int_\Omega w_{h,j} \cdot \nabla_{h,j} u_{h,i} v_{h,i} - \sum_{F \in \mathcal{F}_h^i} \int_F \mathbf{n}_F \cdot \{\mathbf{w}_h\} [\![\mathbf{u}_h]\!] \cdot \{\mathbf{v}_h\}$$
$$+ \frac{1}{2} \int_\Omega (\nabla_h \cdot \mathbf{w}_h)(\mathbf{u}_h \cdot \mathbf{v}_h) - \frac{1}{2} \sum_{F \in \mathcal{F}_h} \int_F \mathbf{n}_F \cdot [\![\mathbf{w}_h]\!] \{\mathbf{u}_h \cdot \mathbf{v}_h\},$$

yielding a non-conservative dG method that contains a source term proportional to the divergence of the discrete velocity (still converging to zero as the mesh is refined). A conservative variant of the advective term discretization requiring the non-standard modification of the pressure field first proposed in [8] has been devised in [13].

Discrete velocity divergence and discrete pressure gradient. The bilinear form associated to the discretization of the velocity divergence in the mass conservation equation is defined, for all $(\mathbf{v}_h, q_h) \in U_h \times P_h$ as

$$b_h(\mathbf{v}_h, q_h) \stackrel{\text{def}}{=} \int_\Omega (\nabla_h \cdot \mathbf{v}_h) q_h - \sum_{F \in \mathcal{F}_h} \int_F \mathbf{n}_F \cdot [\![\mathbf{v}_h]\!] \{q_h\}.$$

Integration by parts yields

$$\begin{aligned} b_h(\mathbf{v}_h, q_h) &= -\int_\Omega \mathbf{v}_h \cdot \nabla q_h + \sum_{T \in \mathcal{T}_h} \sum_{F \subset \partial_T} \int_F \mathbf{v}_h \cdot \mathbf{n}_F q_h - \sum_{F \in \mathcal{F}_h} \int_F \mathbf{n}_F \cdot [\![\mathbf{v}_h]\!] \{q_h\} \\ &= -\int_\Omega \mathbf{v}_h \cdot \nabla q_h + \sum_{F \in \mathcal{F}_h^i} \int_F \mathbf{n}_F \cdot \{\mathbf{v}_h\} [\![q_h]\!] = -\int_\Omega \mathbf{v}_h \cdot \nabla q_h, \end{aligned}$$

where we have used the continuity of the functions in cG(k) to conclude.

Remark 1 (LBB stability). Let, for all $\mathbf{v}_h \in U_h$,

$$\|\mathbf{v}_h\|_{\text{dG}}^2 \stackrel{\text{def}}{=} \sum_{i=1}^d \left(\|\nabla_h v_{h,i}\|_{L^2(\Omega)}^2 + \sum_{F \in \mathcal{F}_h^i} h_F^{-1} \| [\![v_{h,i}]\!] \|_{L^2(F)}^2 \right).$$

That $\|\cdot\|_{\text{dG}}$ is a norm on U_h is a classical result (cf., e.g., Di Pietro and Ern [13]). To check the discrete inf-sup condition, fix $q_h \in P_h$. Following Nečas [23], there exists $\mathbf{v}_{q_h} \in [H_0^1(\Omega)]^d$ such that $\nabla \cdot v_{q_h} = q_h$ almost everywhere in Ω and $\|\mathbf{v}_{q_h}\|_{[H^1(\Omega)]^d} \leq C \|q_h\|_{L^2(\Omega)}$ (C denotes a constant independent of the mesh size h). Then,

$$\begin{aligned} \|q_h\|_{L^2(\Omega)}^2 &= \int_\Omega (\boldsymbol{\nabla} \cdot \mathbf{v}_{q_h}) q_h = -\int_\Omega \mathbf{v}_{q_h} \cdot \nabla q_h \\ &= -\int_\Omega \pi_h \mathbf{v}_{q_h} \cdot \nabla q_h = b_h(\pi_h \mathbf{v}_{q_h}, q_h) \\ &\leq \sup_{\mathbf{w}_h \in U_h} \frac{b_h(\pi_h \mathbf{v}_{q_h}, q_h)}{\|\mathbf{w}_h\|_{\text{dG}}} \|\pi_h \mathbf{v}_{q_h}\|_{\text{dG}} \leq C \sup_{\mathbf{w}_h \in U_h} \frac{b_h(\pi_h \mathbf{v}_{q_h}, q_h)}{\|\mathbf{w}_h\|_{\text{dG}}} \|q_h\|_{L^2(\Omega)}, \end{aligned}$$

where we have used the fact that $P_h \subset V_h^k$ to replace $\mathbf{v}_{q_h}$ with its L^2 projection $\pi_h \mathbf{v}_{q_h}$ onto U_h in the second line and concluded using the H^1 stability of the L^2 projector to bound $\|\pi_h \mathbf{v}_{q_h}\|_{\mathrm{dG}}$ with $\|\mathbf{v}_{q_h}\|_{[H^1(\Omega)]^d}$ (and, hence, with $C\|q_h\|_{L^2(\Omega)}$).

Finally, the bilinear form associated to the time derivative discretization is

$$m_h(\mathbf{u}_h, \mathbf{v}_h) \stackrel{\text{def}}{=} \int_\Omega \mathbf{u}_h \cdot \mathbf{v}_h.$$

The discrete equivalent of equation (10) consist in seeking $\mathbf{u}_h^{n+1} \in U_h$ such that

$$\frac{\beta_0}{\Delta t} m_h(\mathbf{u}_h^{n+1}, \mathbf{v}_h) + \nu a_h(\mathbf{u}_h^{n+1}, \mathbf{v}_h) + t_h(\mathbf{u}_h^n, \mathbf{u}_h^{n+1}, \mathbf{v}_h) + t_h(\mathbf{u}_h^{n+1}, \mathbf{u}_h^n, \mathbf{v}_h) = \int_\Omega \mathbf{f}\mathbf{v}_h - m(u_h^*, \mathbf{v}_h) - b_h(p_h^*, \mathbf{v}_h) + t_h(\mathbf{u}_h^n, \mathbf{u}_h^n, \mathbf{v}_h), \quad \forall \mathbf{v}_h \in U_h, \quad (12)$$

where we have set $u_h^* \stackrel{\text{def}}{=} \frac{\beta_1}{\Delta t}\mathbf{u}_h^n + \frac{\beta_2}{\Delta t}\mathbf{u}_h^{n-1}$ and $p_h^* \stackrel{\text{def}}{=} \gamma_1 p_h^n + \gamma_2 p_h^{n-1} + \gamma_3 p_h^{n-2}$, with the coefficients β_i and γ_i defined in section 2.2. Finally, the discrete problem corresponding to equation (11) consists in seeking $p_h^{n+1} \in P_h$ such that

$$\int_\Omega \nabla_h p_h^{n+1} \cdot \nabla_h q_h = -\frac{\beta_0}{\Delta t} b_h(\mathbf{u}_h^{n+1}, q_h) + \int_\Omega \nabla_h p_h^n \cdot \nabla_h q_h, \quad \forall q_h \in P_h, \quad (13)$$

with the coefficient β_0 defined in section 2.2.

3. Numerical validation

In order to demonstrate the effectiveness of the solution method in the simulation of advection-dominated incompressible flows, we now present temporal and spatial accuracy results obtained for a set of classical benchmark cases.

3.1. Implementation

The solver is implemented using the tools provided by the `libMesh` open source finite element library [25]. For the approximating polynomial space $\mathbb{P}_k(T)$ we use monomials in case of the finite element space V_h^k and Lagrange polynomials for the space Q_h^k. Thus, velocity is approximated with

a modal shape function while pressure is discretized by means of a nodal shape function. The quadrature points are computed by means of a Gaussian quadrature formula and the quadrature order is set so that the mass matrix is exactly integrated. The quadrature order is not increased to take into account exact integration of the non-linear term.

Parallelization is provided by the `libMesh` library at the assembly level, while data structures and algorithms for the parallel solution of sparse linear systems are provided by the `PETSc` toolkit [3]. Both levels make use of the `MPI` communication protocol following a distributed memory model. Mesh partitioning is performed using the `METIS` library or its parallel counterpart `ParMETIS` (`http://glaros.dtc.umn.edu/gkhome/views/metis`).

3.2. Temporal accuracy

In order to confirm the temporal accuracy estimates derived by E and Liu [14], we consider the Taylor vortex test along with the benchmark problem proposed by Couzy [11].

Taylor vortex temporal test. The aim of this test is to demonstrate that the scheme (12)–(13) allows to march in time with high CFL numbers independently of the Reynolds number while preserving the theoretical temporal accuracy. The computational domain consist of the space-time cylinder $\Omega \times (0.1, 6.1)$ with $\Omega = (-\pi/2, \pi/2)^2$. The Dirichlet boundary conditions as well as the initial condition are deduced by the exact solution

$$\begin{aligned} \mathbf{u} &= [-\cos(\pi x)\sin(\pi y)\mathbf{i} + \sin(\pi x)\cos(\pi y)\mathbf{j}]\, e^{-2\pi\nu t}, \\ p &= -\cos(2\pi x)\cos(2\pi y) e^{-4\pi\nu t}, \end{aligned}$$

where $\{\mathbf{i}, \mathbf{j}\}$ denotes the canonical basis of $\mathbb{R}^2$. The space discretization relies on a dG(2)-cG(2) approximation on a very fine 300×300 quadrilateral grid, yielding L^2-projection errors of the order of 10^{-8} for the exact solution $(\mathbf{u}, p)$. The simulations were run with time steps $\Delta t \in \{0.2, 0.1, 0.05, 0.025\}$ and Reynolds number $\mathrm{Re} \in \{10^2, 10^3, 10^4\}$. The results are summarized in Figure 1. The slope of the fit for the velocity and pressure in L^2 norm is 2. The maximum CFL number, corresponding to the largest time step and computed as proposed in [24] for an advection model problem, is about 50. The implicit treatment of the non-linear term allows to choose Δt according to accuracy considerations related to the splitting error and to the physics to be modelled instead of dealing with the stringent stability limit of the advection-diffusion operator.

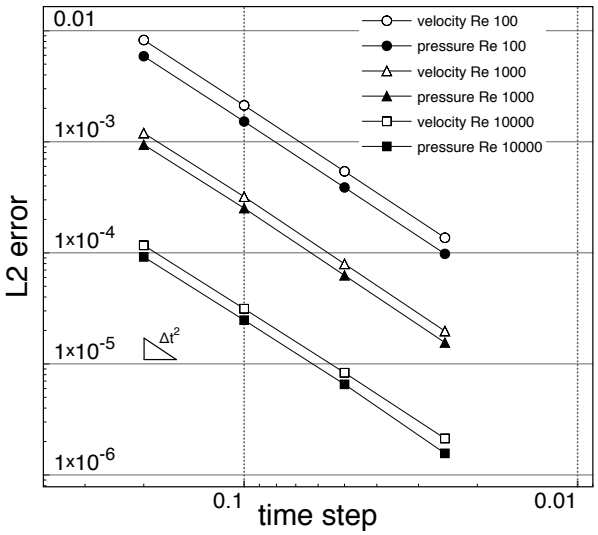

Figure 1: Temporal accuracy of the scheme evaluated using the unsteady Navier-Stokes Taylor vortex analytical solution (see text for details).

Couzy decoupling error temporal test. The second test aimed at assessing the accuracy of the proposed splitting method is the one proposed by Couzy [11]. The INS equations are solved on the time-space cylinder $\Omega \times (0, 0.75)$, with space domain $\Omega = (0, 1)^2 \setminus (0.4, 0.6)^2$ consisting of a square with a hole in the middle. We consider the exact solution

$$\mathbf{u} = [-\cos(\pi x/2)\sin(\pi y/2)\mathbf{i} + \sin(\pi x/2)\cos(\pi y/2)\mathbf{j}]\sin(\pi t),$$
$$p = -\pi \sin(\pi x/2)\sin(\pi y/2)\sin(\pi t).$$

The forcing term as well as the Dirichlet boundary conditions and the initial condition are deduced from the above expression. The problem is discretized in space using dG(2)-cG(2) elements on a fine grid composed by 24,400 quadrilaterals, ensuring that spatial errors are dominated by temporal errors. The L^2 and L^∞ error for both velocity and pressure are evaluated at each time step using increased-order quadrature rules to provide the required accuracy. The simulation is run for Reynolds number $\mathrm{Re} \in \{10, 100, 1000\}$, corresponding to $\nu = \{0.1, 0.01, 0.001\}$. The results are summarized in Figure 2. The slope of the fit for the velocity in L^2 and L^∞ norm and for the pressure in L^2 norm is almost 2, while the order of convergence for the pressure in L^∞ norm is somewhere in between the order of velocity and the order

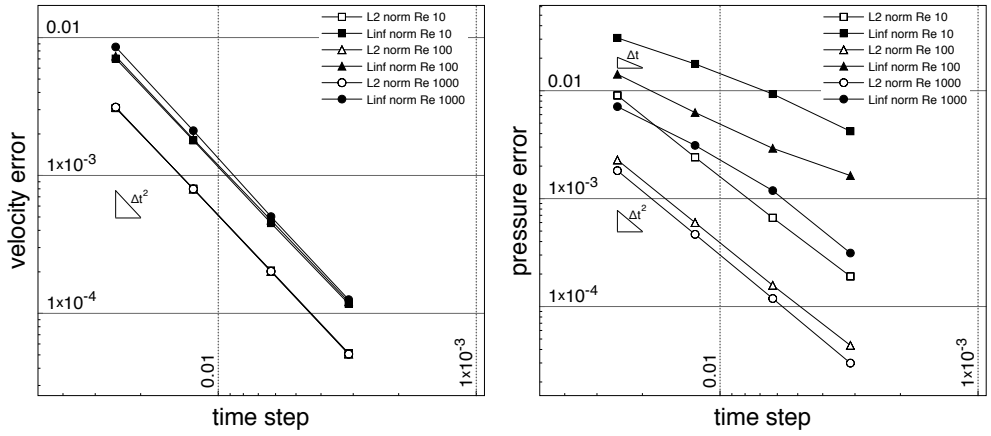

Figure 2: Temporal accuracy of the scheme evaluated on the unsteady Navier-Stokes problem proposed by Couzy (see text for details).

of velocity minus one, confirming the expected convergence rate. Interestingly enough, while the velocity error is almost independent of the Reynolds number, the pressure error decreases with the increase of the Reynolds number. This behavior is referable to the pressure boundary layer due to the artificial Neumann boundary condition derived in equation (9). In the vanishing viscosity limit, equation (9) enforces the consistent boundary condition in equation (4) so that the splitting error limiting the accuracy of the pressure vanishes.

3.3. Spatial accuracy

To numerically assess the spatial convergence rates, we consider the Kovasznay flow [26] in the two-dimensional domain $(-0.5, 1.5) \times (0, 2)$ and the solution proposed by Ethier and Steinman [17] in the three-dimensional domain $(-1, 1)^3$. In these test cases we deal with low Reynolds number flows (as a matter of fact, the Kovasznay solution is similar to the low-speed flow of a viscous fluid past an array of cylinders while the three-dimensional solution consists in a series of counter-rotating vortices involving all three Cartesian velocity components). The exact solution of the Kovasznay flow is given by

$$\mathbf{u} = 1 - e^{\lambda x} cos(2\pi y)\mathbf{i} + \frac{\lambda}{2\pi} e^{\lambda x} \sin(2\pi y)\mathbf{j},$$
$$p = \frac{1}{2}(1 - e^{2\lambda x}),$$

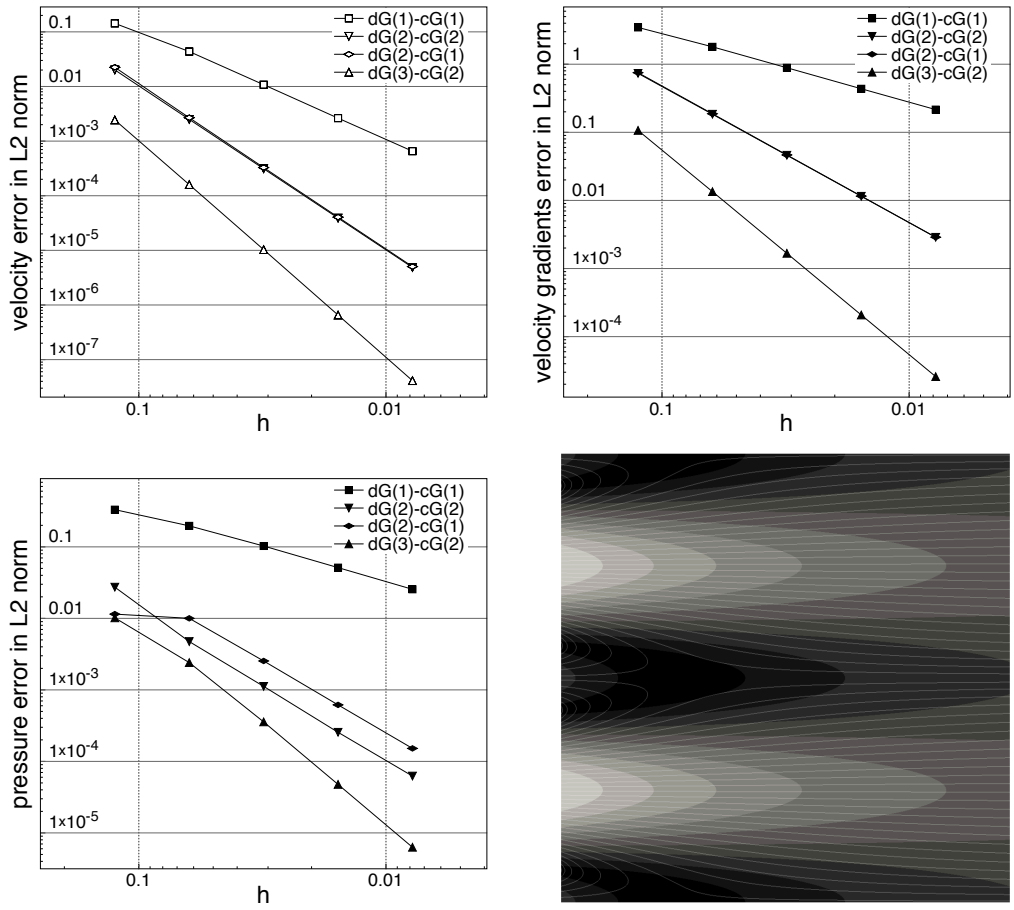

Figure 3: Kovasznay test case. Top row and bottom row left, spatial accuracy of the finite element discretization evaluated on the steady Navier-Stokes problem proposed by Kovasznay (see text for details). Bottom row right, streamlines and velocity contours.

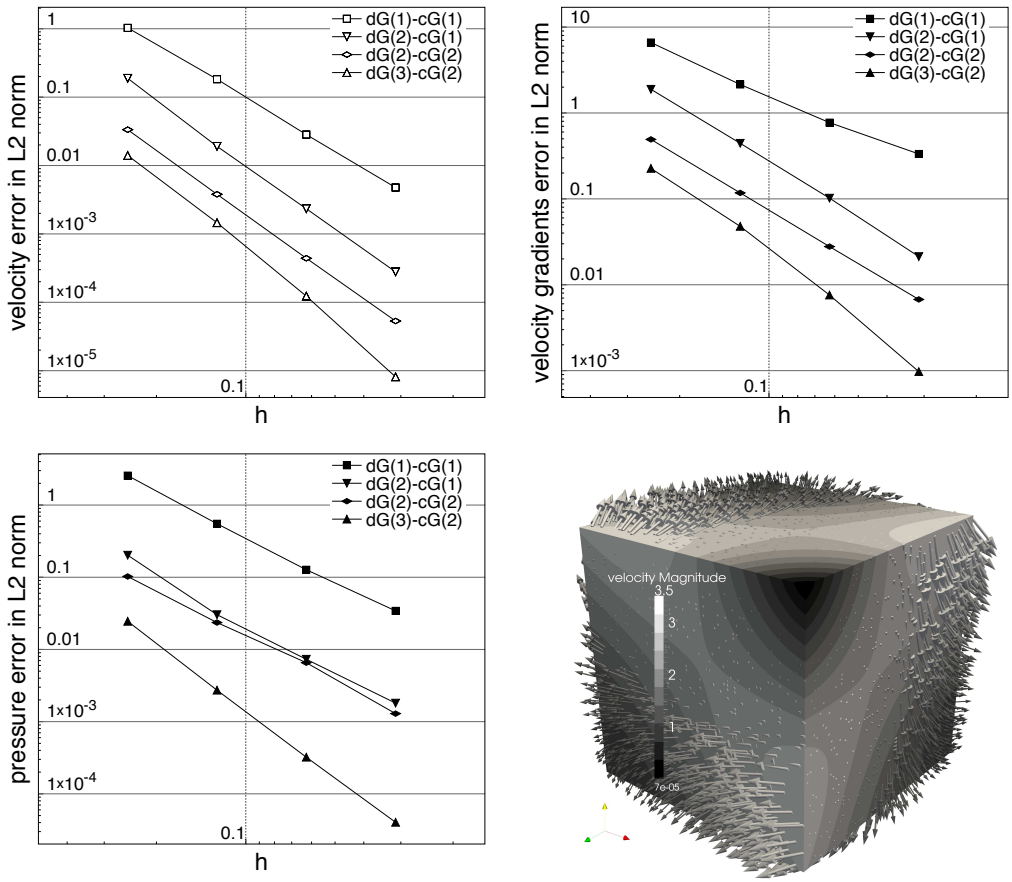

Figure 4: Ethier-Steinman test case. Top row and bottom row left, spatial accuracy of the finite element discretization evaluated on the steady Navier-Stokes problem proposed by Ethier and Steinman (see text for details). Bottom row right, velocity contours and velocity vectors.

where $\lambda = \frac{1}{2\nu} - (\frac{1}{4\nu^2} + 4\pi^2)\frac{1}{2}$. The unsteady analytical solution devised by Ethier and Steinman reads

$$\begin{aligned}
\mathbf{u} = &- a(e^{ax}sin(ay+dz) + e^{az}cos(ax+dy))e^{-d^2t}\mathbf{i} \\
&- a(e^{ay}sin(az+dx) + e^{ax}cos(ay+dz))e^{-d^2t}\mathbf{j} \\
&- a(e^{az}sin(ax+dy) + e^{ay}cos(az+dx))e^{-d^2t}\mathbf{k} \\
p = &- \frac{a^2}{2}(e^{2ax} + e^{2ay} + e^{2az} \\
&+ 2sin(ax+dy)cos(az+dx)e^{a(y+z)} \\
&+ 2sin(ay+dz)cos(ax+dy)e^{a(z+x)} \\
&+ 2sin(az+dx)cos(ay+dz)e^{a(x+y)})e^{-2d^2t},
\end{aligned}$$

where $a = \frac{\pi}{4}$ and $d = \frac{\pi}{2}$. In order to evaluate the spatial convergence without dealing with temporal errors we consider the solution at time $t = 0$ and we add a forcing term balancing diffusion terms in the absence of unsteady terms (while convective terms balance the pressure gradient).

In both test cases we set $\nu = 0.025$ (corresponding to Re $= 40$), Dirichlet boundary conditions are imposed according to the exact solution, while initial conditions over the whole domain corresponds to zero velocity and pressure. In order to obtain a steady-state solution, a pseudo-time integration is performed employing a fixed time step $\Delta t = 0.1$. The L^2 error for both velocity and pressure as well as the L^2 error for the velocity gradients are displayed in Figures 3 and 4. The theoretical convergence rates of h^{k+1} for the L^2 error on the velocity, of h^k for the L^2 error on the pressure and for the L^2 error on the velocity gradients are confirmed for both the dG(k)-cG(k) and dG(k)-cG($k-1$) discretizations. It is interesting to note that in the approximation of the three-dimensional solution proposed by Ethier and Steinman the dG(1)-cG(1) discretization shows a second order convergence rate for the pressure error in L^2 norm while the theoretical convergence rates for the velocity underestimate the numerically evaluated ones by half an order.

Albeit the order of convergence is the same, dG(k)-cG(k) discretizations yield more precise pressure approximations than dG(k)-cG($k-1$) discretizations, scoring a point for equal order finite element spaces implementations. It has to be noticed, however, that the computational effort required by the

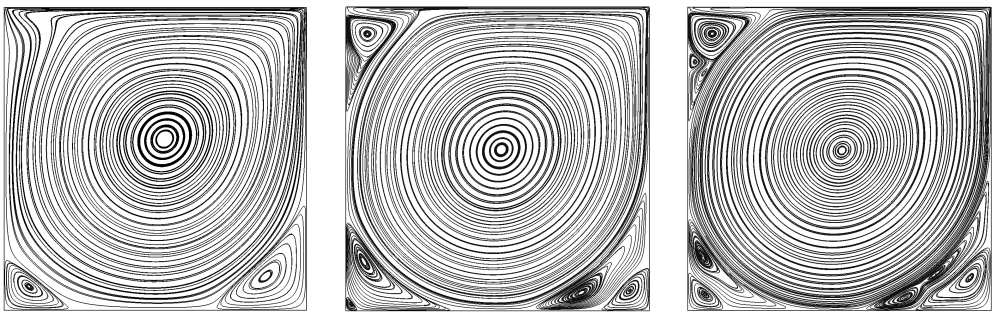

Figure 5: 2D lid-driven cavity test. Streamlines for Re 1000, 10000, 20000.

iterative solution of the projection step accounts for most of the cost of the algorithm, which makes dG(k)-cG($k-1$) discretizations more efficient. Unlike the advection-diffusion step, the number of iterations required by the projection step strongly increases moving from $k = 1$ to $k = 2$ revealing the need of better preconditioning techniques for higher-order pressure discretizations.

3.4. 2D and 3D lid-driven cavity

As a final test case, we consider the two- and three-dimensional lid-driven cavity flow. The computational domain for this problem is a square (a cube in 3D) with edges of unit length. The top side of the cavity slides with a constant imposed velocity, while no-slip Dirichlet boundary conditions are imposed on the remaining sides. Despite its simple geometry, this lid-driven cavity flow presents complex flow patterns due to multiple recirculating secondary vortices at the corners of the cavity, see Figure 5. The space discretization is based on dG(2)-cG(1) elements on a 120×120 quadrilateral grid in 2D and a $50 \times 50 \times 50$ hexahedral grid in 3D. The simulation is advanced in time adopting a pseudo-time integration with fixed time step $\Delta t = 0.1$ until a steady-state is reached.

We present 2D lid-driven cavity solutions at Reynolds number Re = 1000, Re = 10000, and Re = 20000 and compare them with the accurate reference solutions presented in [16]. In that work the values of the two components of the velocity are tabulated along the horizontal and vertical centerlines for Re $\leq$ 21000. These reference solutions have been obtained on a very fine uniform grid of 601×601 with a streamfunction and vorticity formulation of the Navier-Stokes equations. In Figure 5 it can be appreciated that velocity profiles match the reference solutions for all the Reynolds numbers here

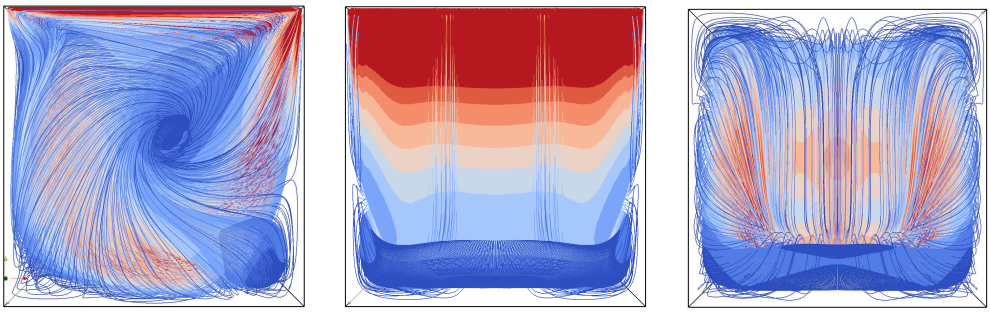

Figure 6: 3D lid-driven cavity test, Re 1000. Streamlines color-coded by velocity magnitude. Side, front and bottom view.

considered. As the Reynolds number increases, the gradient of the velocity at the boundary layers becomes stronger and the number of recirculating vortices at the corners on the cavity increases. In these cases, the accuracy of the solution critically depends on modeling the shear layer along the lid and the discontinuity in the boundary condition at the upper right and left corner.

The 3D lid-driven cavity solution is computed at Reynolds number $\mathrm{Re} = 1000$, and compared with the velocity results tabulated along the x-axis and y-axis in [1]. In that paper the solutions were computed employing a projection method coupled to a fifth-order accurate Chebyshev collocation discretization on a $96 \times 96 \times 64$ hexahedral mesh. In Figures 6 and 7 the symmetry of the streamlines and the perfect agreement between the velocity profiles can be appreciated.

Overall, these results demonstrate that high levels of accuracy can be reached for shear-driven flows at high Reynolds numbers using a projection method.

4. Conclusions

We have presented an efficient and robust INS solver for high-Reynolds unsteady flows. Efficiency is ensured by the use of a projection method to decouple the momentum conservation equation from the incompressibility constraint, thereby allowing an effective solution process based on standard preconditioned iterative solvers. Robustness regards to the Reynolds number is guaranteed by the fully implicit dG discretization of the advection-diffusion

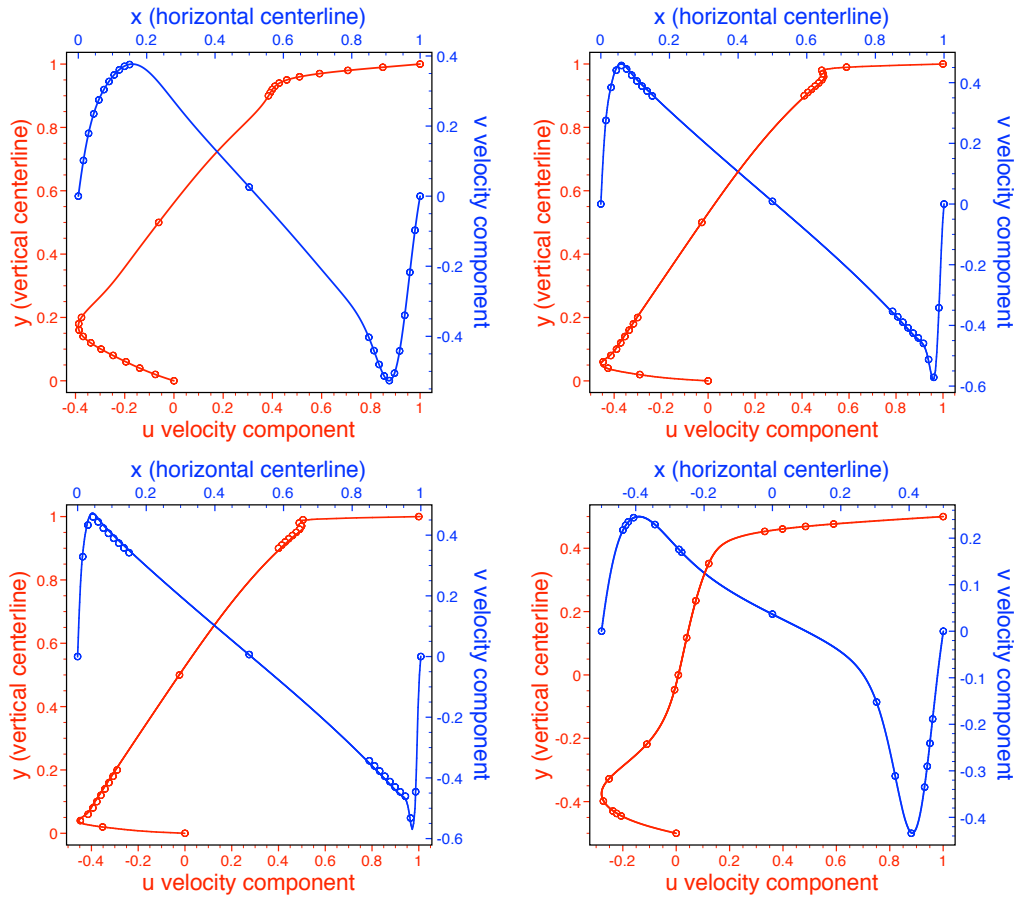

Figure 7: Lid-driven cavity test. Plots of horizontal (red) and vertical (blue) velocity components along the vertical and horizontal centerlines respectively. Top row and bottom row left, 2D lid-driven cavity at Re 1000, 10000 and 20000: the dots correspond to the reference values provided by Erturk et al [16]. Bottom row right, 3D lid-driven cavity at Re1000: the dots correspond to the reference values provided by Albensoeder et al [1].

step.

We demonstrated the ability to accurately resolve 2D and 3D challenging benchmark problems in moderate to high Reynolds numbers flow regimes with time steps larger than the ones imposed by the CFL stability limit. The possibility to manage hybrid grids can be exploited to extend the solver applicability to complex geometries as the ones required for hemodynamic simulations. An open-source hemodynamics solver based on the proposed algorithm will be the subject of future work.

Acknowledgements

The authors are thankful to Luca Antiga (Mario Negri Institute for Pharmacological Research) for fruitful discussions. The research leading to these results has received funding from the European Community's Seventh Framework Programme (FP7/2007-2013:ARCH, Project n.224390).

References

[1] S. Albensoeder, H. C. Kuhlmann, Accurate three-dimensional lid-driven cavity flow, J. Comp. Phys. 206 (2005) 536-558.

[2] D. N. Arnold, An Interior Penalty Finite Element Method with Discontinuous Elements, SIAM J. Num. Anal. 19 (1982) 742-760.

[3] S. Balay, K. Buschelman, V. Eijkhout, W. Gropp, D. Kaushik, M. Knepley, L. C. McInnes, B. Smith, H. Zhang, PETSc Users Manual, Argonne National Laboratory, Mathematics and Computer Science Division, 2.3.3 edn.

[4] F. Bassi, A. Crivellini, D. A. Di Pietro, S. Rebay, An artificial compressibility flux for the discontinuous Galerkin solution of the incompressible Navier-Stokes equations, Comp. Phys. 218 (2006) 794-815.

[5] F. Bassi, A. Crivellini, D. A. Di Pietro and S. Rebay, An implicit high-order discontinuous Galerkin method for steady and unsteady incompressible flows, Comp. & Fl. 36(10) (2007) 1529–1546

[6] A. J. Chorin, Numerical solution of the Navier-Stokes equations, Math. Comp. 22 (1968) 745–762.

[7] B. Cockburn, G. Kanschat, D. Schötzau, The local discontinuous Galerkin method for the Oseen equations, Math. Comp. 73 (2003) 569-593.

[8] B. Cockburn, G. Kanschat, D. Schötzau, A locally conservative LDG method for the incompressible Navier-Stokes equations, Math. Comp. 74 (2005) 1067-1095.

[9] B. Cockburn, G. Kanschat, D. Schötzau, and C. Schwab, Local Discontinuous Galerkin methods for the Stokes system, SIAM J. Numer. Anal. 40 (2002), 319-343.

[10] B. Cockburn, C.-W. Shu, Runge-Kutta discontinuous Galerkin methods for convection-dominated flows, J. Sci. Comp. 16 (2001) 173-261.

[11] W. Couzy, Spectral element discretization of the unsteady Navier-Stokes equations and its iterative solutions o parallel computers, PhD Thesis, École Polytechnique Fédérale de Lausanne, 1995.

[12] D. A. Di Pietro, Analysis of a discontinuous Galerkin approximation of the Stokes problem based on an artificial compressibility flux, Int. J. Numer. Meth. Fluids 55 (2007) 793–813.

[13] D. A. Di Pietro, A. Ern, Discrete functional analysis tools for discontinuous Galerkin methods with application to the incompressible Navier-Stokes equations, Math. Comp. (2010). To appear. Preprint available at `http://hal.archives-ouvertes.fr/hal-00278925/fr/`.

[14] W. E, J.-G. Liu, Projection method I: Convergence and numerical boundary layers. SIAM J. Numer. Anal. 32 (1995) 1017-1057.

[15] W. E, J.-G. Liu, Gauge method for incompressible flows, Comm. Math. Sci. 1 (2003) 317-332.

[16] E. Erturk, T. C. Corke, C. Gökçöl, Numerical Solutions Of 2-D Steady Incompressible Driven Cavity Flow At High Reynolds Numbers, Inti. J. Num. Meth. Fluids 48 (2005) 747-774.

[17] C. R. Ethier, D. A. Steinman, Exact Fully 3D Navier-Stokes Solutions for Benchmarking, Inti. J. Num. Meth. Fluids 19 (1994) 369-375.

[18] H. Georgoulis, E. Süli, Optimal Error Estimates for the *hp*-Version Interior Penalty Discontinuous Galerkin Finite Element Method, J. Sci. Comp. 30 (2007) 465-491.

[19] V. Girault, B. Rivire, and M. F. Wheeler, A discontinuous Galerkin method with nonoverlapping domain decomposition for the Stokes and Navier-Stokes problems, Math. Comp. 74 (2004) 53-84.

[20] K. Goda, A multistep technique with implicit difference schemes for calculation two- or three-dimensional cavity flows, J. Comp. Phys. 30 (1979) 76-95.

[21] J.-L. Guermond, L. Quartapelle, On stability and convergence of projection methods based on pressure poisson equation, Int. J. Num. Meth. Fluids, 26 (1998) 1039-1053.

[22] J. L. Guermond, P. Minev, J. Shen, An overview of projection methods for incompressible flows, Comp. Meth. Appl. Mech. Engrg. 195 (2006) 6011-6045.

[23] J. Nečas, Equations aux dérivées partielles, Presses de l'Université de Montréal, Montréal, Canada, 1965.

[24] G. E. Karniadakis, S. Sherwin, Spectral/*hp* Element Methods for Computational Fluid Dynamics, Oxford Science Pupplications, 2004.

[25] B. Kirk, J. W. Peterson, R. H. Stogner, G. F. Carey, libMesh: A C++ Library for Parallel Adaptive Mesh Refinement/Coarsening Simulations Boundary conditions for incompressible flows, Eng. Comput. 22 (2006) 237-254.

[26] L. I. G. Kovasznay, G. Taylor, Laminar flow behind a two-dimensional grid, Proc. Camb. Phil. Soc. 44 (1948) 58.

[27] J.-G. Liu, C.-W. Shu, A High-Order Discontinuous Galerkin Method for 2D Incompressible Flows, J. Comp. Phys. 160 (2000) 577-596.

[28] S. A. Orszag, Spectral methods for problems in complex geometries, J. Comp. Phys. 37 (1980) 70-92.

[29] K. Shahbazi, P. F. Fischer, C. R. Ethier, A high-order discontinuous Galerkin method for the unsteady incompressible Navier-Stokes equations, J. Comp. Phys. 222 (2007) 391-407.

[30] J. Shen, On error estimates of projection methods for the Navier-Stokes equations: second-order schemes, Math. Comput. 65 (1996) 1039-1065.

[31] R. Temam, Sur l'approximation de la solution des quations de Navier-Stokes par la mthode des pas fractionnaires, Arch. Ration. Mesh. Anal. 33 (1969) 377-385.

[32] J. Van Kan, A second-order accurate pressure-correction scheme for viscous incompressible flow, SIAM J. Sci. Stat. Comp. 7 (1986) 870-891.